Geomechanics and Engineering, *Vol. 24, No. 2 (2021) 179-191*
DOI: https://doi.org/10.12989/gae.2021.24.2.179

Failure characteristics and mechanical mechanism of study on red sandstone with combined defects

Bing Chen[1a], Zhiguo Xia*[1], Yadong Xu[1], Shuai Liu[2] and Xingzong Liu[3]

[1]*State Key Laboratory of Mining Disaster Prevention and Control Co-founded by Shandong Province and the Ministry of Science and Technology, No.579, Qianwangang Road, Huangdao District, Qingdao, Shandong Province,266590, China*
[2]*College of Earth Resource Sciences and Engineering, North China University of Water Resources and Electric Power, No.136, Jinshui Dong Road, Zhengzhou, Henan Province,450045, China*
[3]*College of Civil Engineering, Lu Dong University, No. 186, Hong qi Middle Road, Zhifu District, Yantai, Shandong Province, 264025, China*

(Received September 21, 2020, Revised January 7, 2021, Accepted January 8, 2021)

Abstract. In this study, the strength and failure mechanism of red sandstones with combined defects were investigated by uniaxial compression tests on red sandstones with different crack angles using two-dimensional particle flow code numerical software, and their mechanical parameters and failure process were studied and analyzed. The results showed that the mechanical characteristics such as peak strength, peak strain, and elastic modulus of the samples with prefabricated combined defects were significantly inferior than those of the intact samples. With increasing crack angle from 15° to 60°, the weakening area of cracks increased, elastic modulus, peak strength, and peak strain gradually reduced, the total number of cracks increased, and more strain energy was released. In addition, the samples underwent initial brittle failure to plastic failure stage, and the failure form was more significant, leading to peeling phenomenon. However, with increasing crack angle from 75° to 90°, the crack–hole combination shared the stress concentration at the tip of the crack–crack combination, resulted in a gradual increase in elastic modulus, peak strain and peak strength, but a decrease in the number of total cracks, the release of strain energy reduced, the plastic failure state weakened, and the spalling phenomenon slowed down. On this basis, the samples with 30° and 45° crack-crack combination were selected for further experimental investigation. Through comparative analysis between the experimental and simulation results, the failure strength and final failure mode with cracks propagation of samples were found to be relatively similar.

Keywords: numerical test; crack-crack combination; cracks-hole combination; acoustic emission count; crack propagation

1. Introduction

The stability of rock mass structure is very important for the construction of rock mass engineering; however, the presence of cracks, holes, and other defects in the natural rock mass seriously weakens the strength of rock and dominates the rock failure and instability characteristics, thus seriously restricting the orderly development of rock mass engineering such as tunnels, reservoirs, and mines. The stability of rock mass structure has been carried out extensively. Previous studies mainly focused on rock mass with single crack and other defects, multi cracks and other combined defects, leading to fruitful results.

In the study of rock masses with a single crack and other defects, Mondal *et al.* (2019) discussed the damage evolution and fracture propagation process of three-dimensional pre-cracked sandstone specimens under uniaxial compression by numerical simulation. Gratchev *et al.* (2016) studied the effects of length and width of a flaw on the strength of rock-like specimens. Shi *et al.* (2019) thought that the prefabricated cracks significantly weakened the rock and the weakening became more obvious with increasing total length of the prefabricated cracks. Through the indoor uniaxial compression test, Wong *et al.* (2006) found that the diameter of a single prefabricated hole has an obvious effect on the strength of samples, and the larger the diameter of the prefabricated hole is, the smaller the strength of the specimen is. Bastola *et al.* (2019) carried out uniaxial compression experiment and found that a combination of wing, anti-wing, shear, and secondary cracks were observed in the models with pre-existing planar cracks, but complex cracking mechanism was observed in the models with pre-existing nonplanar cracks. Through the indoor uniaxial compression tests, Du *et al.* (2016) found that the peak strength of samples decreased exponentially with increasing ratio of the long axis to the short axis. By means of uniaxial compression test, Zhu *et al.* (2019) found that hole defects of different shapes have different weakening effects on the strength of rock samples. Chen *et al.* (2020) studied the strength and failure characteristics of ten types of prefabricated hole defective rocks by numerical simulation. Xia *et al.* (2020) thought that the presence of inclusions can improve the mechanical properties of defective rock.

*Corresponding author, Ph.D.
E-mail: 514579197@qq.com
[a]Ph.D. Student
E-mail: cdbakdw@163.com

ISSN: 2005-307X (Print), 2092-6219 (Online)

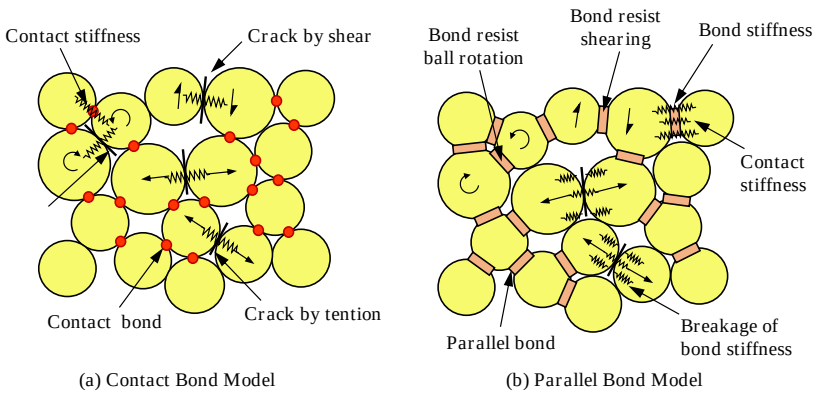

(a) Contact Bond Model (b) Parallel Bond Model

Fig. 1 Cohesive model and its micro-mechanical behavior schematic diagram (a) CB model and (b) PB model

In the study of rock masses with multiple cracks or multiple holes and other combined defects, Lee *et al.* (2011) studied cracks propagation and coalescence of two non-parallel prefabricated cracks and classified them by the characteristics of crack coalescence. Based on micromechanics, a compression dynamic failure model for brittle materials with circular defects is proposed and its accuracy was verified successfully by Katcoff *et al.* (2014). Li *et al.* (2013) studied crack coalescence law of rock samples with a pair of parallel prefabricated cracks by numerical simulation software, and 11 typical coalescence modes were summarized. Through laboratory tests, Morgan *et al.* (2017) found that the position relationship between the bedding plane and the maximum loading force determined the direction of cracks propagation. Based on uniaxial compression tests of sandstone with three prefabricated cracks, Yang *et al.* (2012) established the relationship between the real-time coalescence process of cracks and the axial stress-strain, which could accurately evaluate the deformation characteristics of rocks with prefabricated cracks. Hadi *et al.* (2015) studied the crack propagation mechanism of rock-like materials with rectangular holes by laboratory tests and numerical simulation. Asadizadeh *et al.* (2018) conducted a study using square rock-like blocks containing two parallel preexisting rough non-persistent cracks and found that the uniaxial compressive strength and elastic modulus increase with increasing joint roughness coefficient, bridge length and bridge angle. By studying the fracture behavior and coalescence process of two non-parallel overlapping defects, Afolagboye *et al.* (2017) found that the coalescence tensile crack and tensile wing cracks were the first cracks to develop from the preexisting flaws. Huang *et al.* (2019) investigated the effect of the geometry of pre-existing holes on the strength and fracture behaviors of rock and rock-like samples with prefabricated cracks-hole combination by uniaxial compression tests. Liu *et al.* (2017) found that the strength and elastic modulus of samples increased with increasing defect inclination angle. Sarfarazi *et al.* (2018) found that the tensile strength of the rock decreases with increasing number of prefabricated holes. Vahab *et al.* (2018) studied the crack initiation and failure behavior of an array pattern and random pattern with different hole spacing distributions by physical test. Wong *et al.* (2015) studied the crack propagation and stress changes in heterogeneous rocks with multiple holes by a numerical simulation software RFPA3D.

Based on the joint efforts of various scholars in this and related fields (Bratov *et al.* 2019, Aharonov *et al.* 2019, Saadati *et al.* 2016, Zaitsev *et al.* 1981, Liu *et al.* 2019, Xu *et al.* 2020, Zhao *et al.* 2020), the problems in rock mass engineering such as tunnels, reservoirs, and mines have been satisfactorily solved, ensuring the life safety of construction personnel. However, because of the widespread existence of cracks, holes, and other defects in natural rock mass, and their forms are complex, and the combination of cracks and holes and other defects not only exist in a single form, but also in the form of combination. When the distance between the defects group is relatively close, the interaction between them will seriously affect the stability of rock mass structure and pose a great threat to engineering excavation. This problem has not been given enough attention. Therefore, on the basis of previous studies, in this study, red sandstone was selected as the research object, and the interaction between crack–crack combination and crack-hole combination was used as an example using two-dimensional particle flow code (PFC2D) numerical simulation software to simulate the rock with different angle defects combination, and the effect of rocks with different angle combination defects on the mechanical parameters, failure characteristics, and cracks propagation law was investigated. At the same time, the indoor uniaxial compression tests of rocks with two types of angle defective combination were carried out, and the results were compared with the results of numerical simulation. This study has a certain guiding significance for the construction in the field of underground engineering.

2. Numerical simulation experiment

2.1 Particle flow code

Cundall and Strack (2008) established the particle flow theory of the particle flow code. The basic components of the PFC2D program are particles and bond. Discrete particles are rigid particles with normal and tangential stiffness, and the contact bond (CB) and parallel bond (PB)

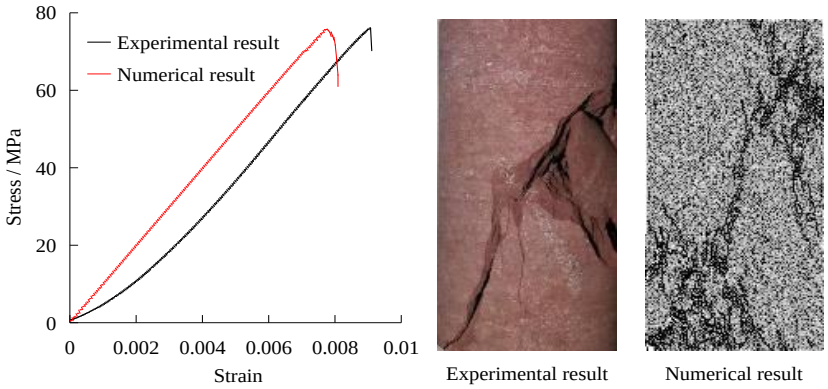

Fig. 2 Comparison of calibration numerical results and experimental results

Table 1 Physical and mechanical parameters of sandstone model

Parameter	Value	Parameter	Value
Minimum particle diameter (mm)	0.3	Porosity	0.1
Particle diameter ratio	1.5	Parallel bond friction angle (°)	37
Density (kg/m^3)	2480	Parallel bond tensile strength (MPa)	23.8
Contact modulus of the particle (GPa)	4.35	Normal critical damping ratio	0.5
Contact bond gap (mm)	0.05	Parallel bond cohesive force (MPa)	33.8

are the two bond modes (Cho *et al.* 2007, Lisjak and Grasselli 2014), as shown in Fig. 1. PB can transfer forces and moment between particles, while CB can only transfer forces acting on the contact points, but cannot transfer moment. Parallel bond model (PBM) was found more suitable for simulating rock materials. Therefore, in this study, uniaxial compression model of rock specimen was modeled by PBM.

2.2 Determination of microscopic parameters

Microscopic physico-mechanical parameters of the particles and the bond properties are required for running the simulation tests using the particle flow theory. The macroscopic mechanical properties of the rock should be reproduced by the generated microscopic parameters. Therefore, the determination of microscopic parameters is crucial. Based on the experimental study, a large number of numerical simulation similar to the laboratory experiment was performed, and the numerical simulation results were compared to the experimental results. The microscopic parameters were adjusted repeatedly by "trial and error" method until they satisfied the requirement of simulation analysis (Xu *et al.* 2020). Fig. 2 shows the comparison between the final calibration results of the experimental and the numerical simulation results, indicating that the stress–strain curve shape and failure mode are relatively similar. Therefore, the final microscopic parameters were determined, as listed in Table 1.

2.3 Establishment of the numerical model with different crack angle combined defects

In order to study the failure characteristics and mechanical properties of rock with different crack angle combination defects, the numerical model of rock with different crack angle defects was established. The angle between two cracks on the upper right side was defined as the crack angle. In this experiment, the height of model was 100 mm, and the width was 50 mm. Seven models with crack angles α of 15°, 30°, 45°, 60°, 75°, and 90° were established. The vertical crack on the upper right side of the model was 5 mm from the right boundary, the intersection of the two cracks was 20 mm from the upper boundary, and the distance between the center of the hole and the bottom and the left was 30 mm and 15 mm, respectively. The geometry of the cracks and circular holes is defined by four geometric parameters: (i) the upper right cracks length (L), (ii) the angle between two cracks (α), (iii) the diameter of circular hole (d), and (iv) the cracks (a) connected to the circular hole, and as shown in Fig. 3. In order to study the

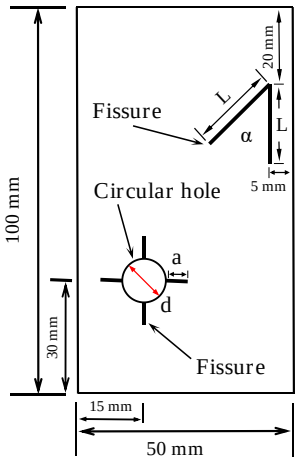

Fig. 3 Schematic diagram of the model

Table 2 Parameters of sandstone samples with cracks and defects combination under uniaxial compression

Sample	W/ (mm)	H/ (mm)	α (°)	L (mm)	a (mm)	d (mm)
①	50	100	15	20	5	10
②	50	100	30	20	5	10
③	50	100	45	20	5	10
④	50	100	60	20	5	10
⑤	50	100	75	20	5	10
⑥	50	100	90	20	5	10

Note: W=Width; H=Height

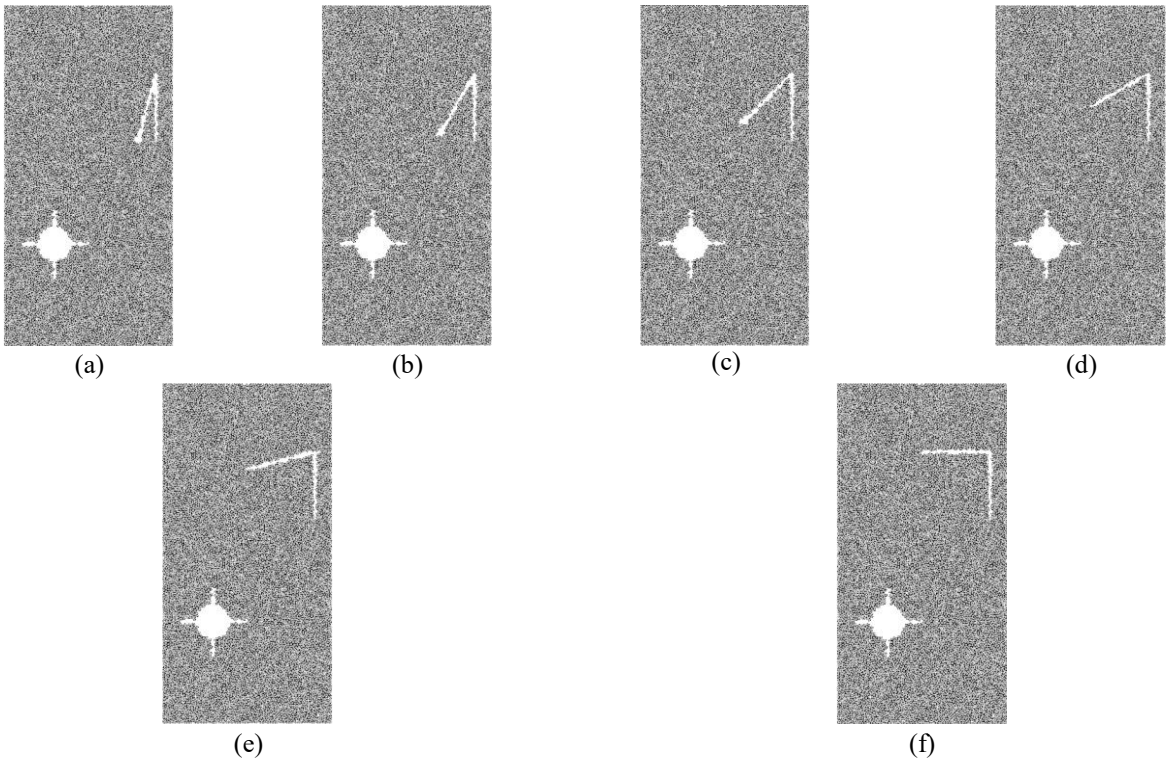

Fig. 4 Numerical model samples of different angle crack and defect combination (α = 15°, 30°, 45°, 60°, 75°, and 90°)

effect of geometry of different prefabricated cracks on the strength, deformation, and failure behavior of sandstone under uniaxial compression, the angle between two cracks α (the angle between the upper right two cracks in Fig. 5) was changed, while the other three parameters were kept unchanged (L = 20 mm, a = 5 mm, d = 10 mm). Table 2 shows the description of sandstone samples with different crack angle defect geometry. First, a complete rock model was established according to the parameters listed in Table 1, and then the particles in the complete rock model were deleted according to the location and size of defect crack combination (circle holes and cracks) shown in Fig. 3, thus forming a rock numerical model with different fracture angles, as shown in Fig. 4. (In the Figure, the upper right side defect was called the crack-crack defect combination, and the left lower side defect was called the crack-hole defect combination, and both of them were collectively called as the crack and defect combination.)

2.4 Analysis of numerical experimental results

2.4.1 Influence of cracks angle on strength and deformation parameters of sandstone

Fig. 5 shows the curve of the relationship between stress, cracks number, and strain in the numerical model of rock with different cracks angle. The stress-strain curve of each angle in the figure was consistent with the corresponding cracks-strain curve, indicating that the stress-strain curve and the change rule of the number of cracks in rock with different angle defects were roughly the same. Because the particles in the PFC2D model were rigid and could not simulate the elastic stage of real rock, the compaction closure stage of the real rock was not reproduced in the numerical model, but the plastic deformation and failure stage can be well reproduced in the numerical model. This characteristic of PFC2D solved the problem of rock discreteness and was helpful to study the effect of crack defects on the rock mechanical properties and cracks failure characteristics (Damaskinskaya *et al.* 2018, Chen *et al.* 2020, Lv *et al.* 2020, Xue *et al.* 2020). As shown from the cracks number curve in the figure, during

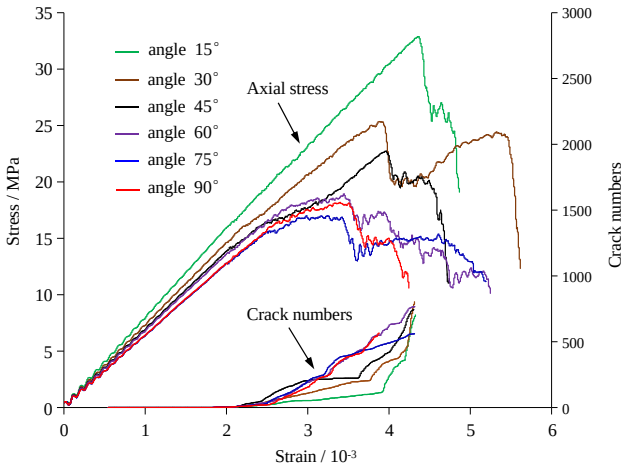

Fig. 5 Stress-strain curve and strain-cracks curve of rock with different cracks angle defects

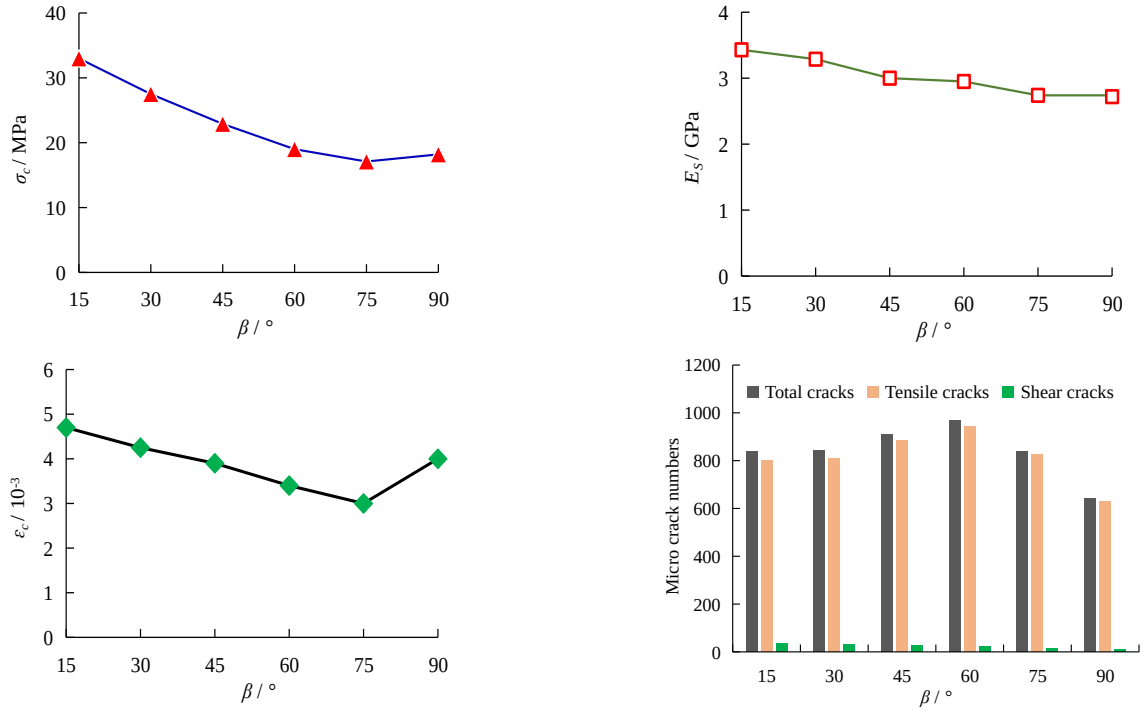

Fig. 6 Effect of cracks angle on strength, deformation parameters, and microcracks number of defective siltstone samples

the initial loading stage, the cumulative number of cracks was zero, and this was inconsistent with the experimental results of real rock, because the particles in PFC2D were rigid bodies, and the PB did not break during the initial loading stage. With increasing axial strain, the number of micro-cracks increased, but the growth rate was slow. When the axial strain was greater than 0.025, the growth rate of cracks was faster, and the total cracks number increased first and then decreased with increasing crack angle. When crack angle was 60°, 75°, and 90°, the number of cracks was larger than that when the crack angle was 15°and 30°. At the same time, the strain needed to reach the peak strength was smaller. When cracks angle was 15° and 30°, the number of cracks in the slow crack growth stage was the least, while that in the rapid growth stage increased rapidly, and the strain required to reach the peak strength was larger. When crack angle was 45°, the cracks propagation was between the two. The early slow growth stage was similar to that when the crack angle was 60°, 75°, and 90° and tended to be smooth in the middle stage, and then became similar to 15°and 30° cracks propagation. However, with increasing crack angle, the stress–strain characteristics were relatively discrete, and the plastic stage of the stress-strain curve gradually tended to smooth, and there were several peaks after the peak value, showing a sawtooth shape.

Fig. 6 shows the effect of crack angle on the strength, deformation parameters, and the number of microcracks in defective sandstone, indicating that the peak strength of crack angles at 15°, 30°, 45°, 60°, 75°, and 90° were 33, 27.5, 22.9, 19, 17.1, and 18.2 MPa, respectively. With the change in angle from 15° to 75°, the peak strength decreased gradually, but increased slightly when crack

angle was 90°. This may be due to the fact that one of the cracks was perpendicular to the axial stress, and the vertical stress acted uniformly on the upper part of the crack. At the same time, the cracks-holes combination shared the stress at the tip of the cracks-cracks tip and weakened the stress concentration. Fig. 2 shows that the peak strength of the complete sample was approximately 73.6 MPa, which was significantly higher than the peak strength of rock with cracks and defects, indicating that the combination of cracks and defects has a greater impact on the rock strength.

With increasing crack angle, the elastic modulus of samples decreased gradually. The difference in the elastic modulus between 15° and 30° was small. The elastic modulus between 45° and 60° was basically the same, and also the same between 75° and 90°. The ratio in the difference in the elastic moduli between groups was about 4.1%, 1.66%, and 0.7%. The histogram of the number of microcracks in Fig. 6 further illustrates the effect of crack angle on the number of microcracks in crack composite samples under uniaxial compression, indicating that the number of tensile microcracks was much higher than the number of shear microcracks, and the number of microcracks depended on the crack angle. With increasing crack angle, the number of microcracks increased first and then decreased.

In defect composite samples with the cracks angle in the range 15°-75°, the peak strength, elastic modulus, and peak strain decreased with increasing crack angles, and increased slightly when cracks angle was 90°. The number of microcracks increased gradually when the crack angle was between 15° and 60°, but decreased after 60°.

2.4.2 Cracks evolution characteristics of rock with different angle defects

Fig. 7 shows the crack evolution process of rock samples with different cracks angle defects. The propagation of initial cracks form of rock with different crack angles in Fig. 8 clearly shows that with increasing crack angle, cracks appeared at the upper and lower tips of crack–hole combination and crack-crack combination. When the simulation test was carried out to step 2.9/104, there were obvious differences in the propagation of cracks of rock with different cracks angle. When cracks angle was 15° and 30°, no new cracks appeared, and the original cracks were extended. When crack angle was 45°, many cracks appeared at the left end of cracks-hole combination. When crack angle was 60°, several cracks also appeared at the left end of the crack-hole combination, and a main crack extending downward intersected with the crack at the lower end of the cracks-hole combination. When the crack angle was 75°and 90°, the same rule appeared as that at 60°, but with increasing crack angle, the extension length of cracks increased. When the simulation test was carried out to step 3.6/104, and the crack angle was 15° and 30°, multiple cracks began to appear at the left end of the crack-hole combination and gradually extended to the bottom of the samples. When crack angle was 45°, an upward crack appeared at the left end of the crack-hole combination. At the same time, the spalling phenomenon occurred in the downward direction at the left end of the crack-hole combination. When the crack angle was 45°, with increasing crack angle, the spalling phenomenon in the downward direction of the left end of the cracks–hole combination became more and more obvious. When the simulation test was carried out to step 4/104, the whole instability and failure progress occurred in the defective rock mass with the crack angles of 15°, 30°, 45°, and 60°. However, with increasing cracks angle, the right end of the crack-crack combination of samples gradually showed peeling phenomenon, and the samples underwent extreme failure and instability. When the simulation test was carried out to step 5.1/104, the whole failure progress occurred in the defective rock masses with the crack angles of 75° and 90°, accompanied by spalling phenomenon.

With increasing crack angle from 15° to 60°, the overall failure shape of the sample became more obvious, and the local spalling phenomenon gradually appeared, because with increasing crack angle, the weakening range of crack of rock samples increased, doubling the stress concentration at the tip and near the cracks, further breaking the rock samples. However, when the crack angle increased from 75° and 90°, the crack-hole combination shared part of stress near the crack-crack combination, reduced the stress concentration, and then delayed the failure process of samples.

2.4.3 Influence of defective rock with different cracks angle on acoustic emission characteristics

Fig. 9 shows the relationship curve of axial stress, count, and strain of rock samples with different cracks angle defects, indicating that the evolution characteristics of acoustic emission were closely related to the stress-strain curve. When cracks angle was 15°, at the initial stage of loading, the acoustic emission event was not active and the acoustic emission count was less. The acoustic emission behavior at this stage has nothing to do with the crack angle of defective rock. With the progress of loading test, the rock samples began to enter the elastic stage, and the acoustic emission count increased, but there was no sudden increase. This was mainly due to the development of some microcracks in rock sample and the release of some strain energy. With further increase in loading, the acoustic emission energy was stable; however, when the axial strain reached 4×10^{-3}, the acoustic emission energy increased rapidly mainly due to the nucleation of a large number of microcracks and the appearance of macroscopic cracks. As the loading continued, the acoustic emission energy remained high until the stress-strain curve dropped sharply because after the occurrence of macroscopic cracks, multiple macroscopic cracks developed rapidly and penetrated each other, resulting in the overall instability and failure of sample. When the crack angle was 30°, the stress-strain curve had two peaks. At the initial stage of experimental loading, the acoustic emission characteristics were the same as that at the crack angle of 15°. When the test reached the first peak, the acoustic emission energy value increased sharply, mainly because the local macroscopic cracks penetrated each other, leading to the local spalling of sample, the strain energy was released, leading to the sudden increase in the strain energy. After the

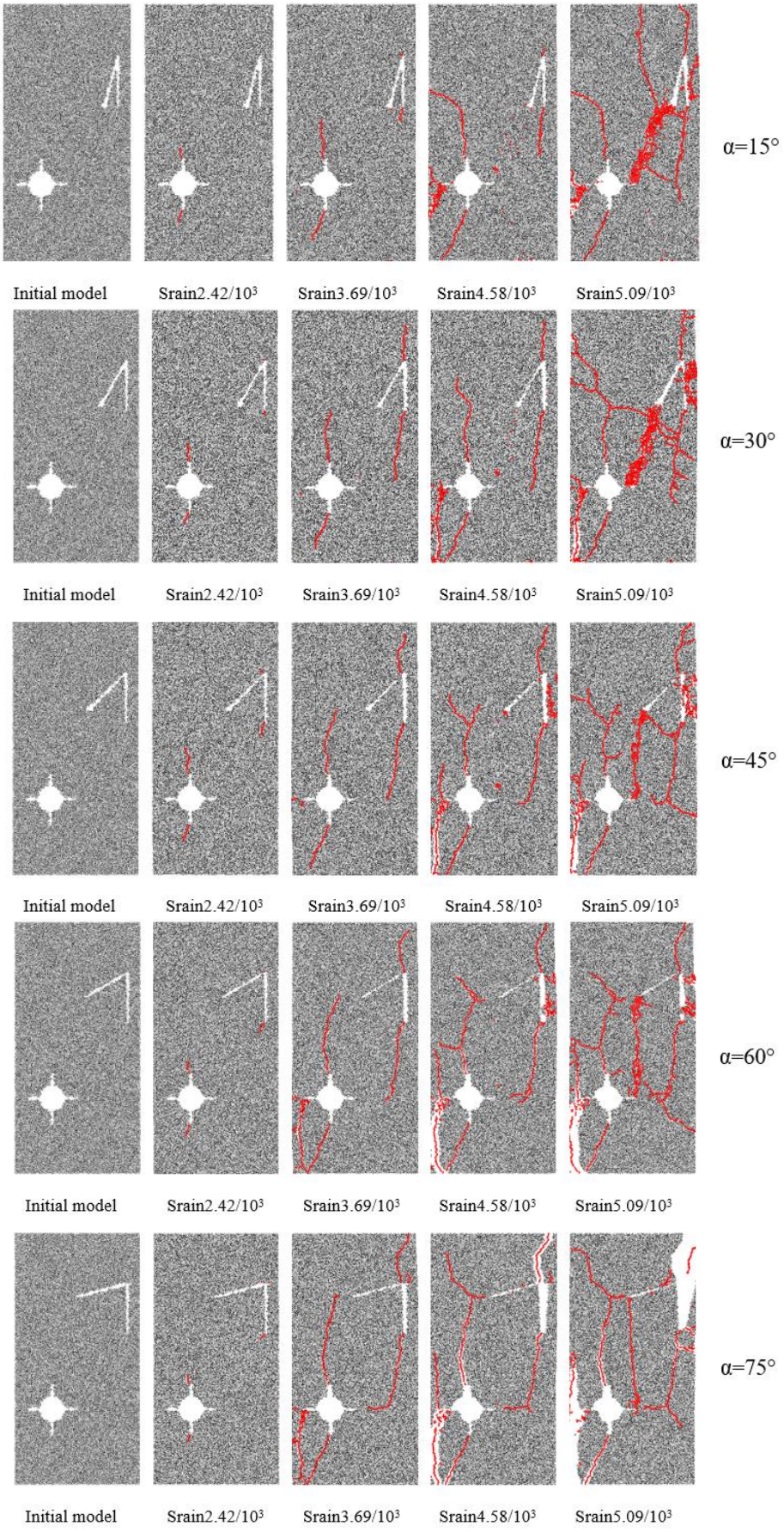

Fig. 7 Crack evolution process of rock with different angle defects

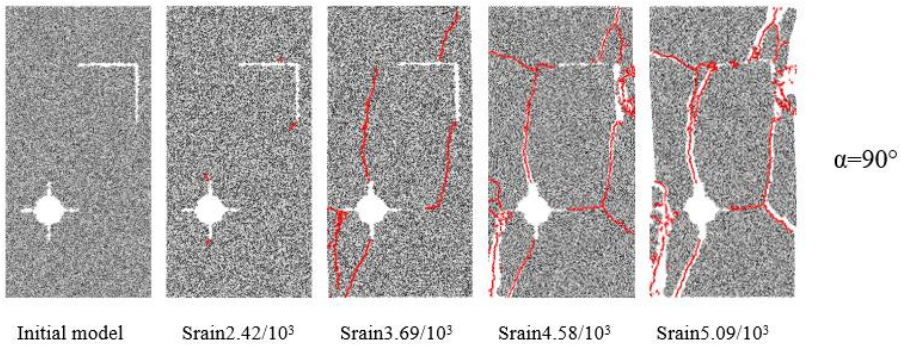

Fig. 7 Continued

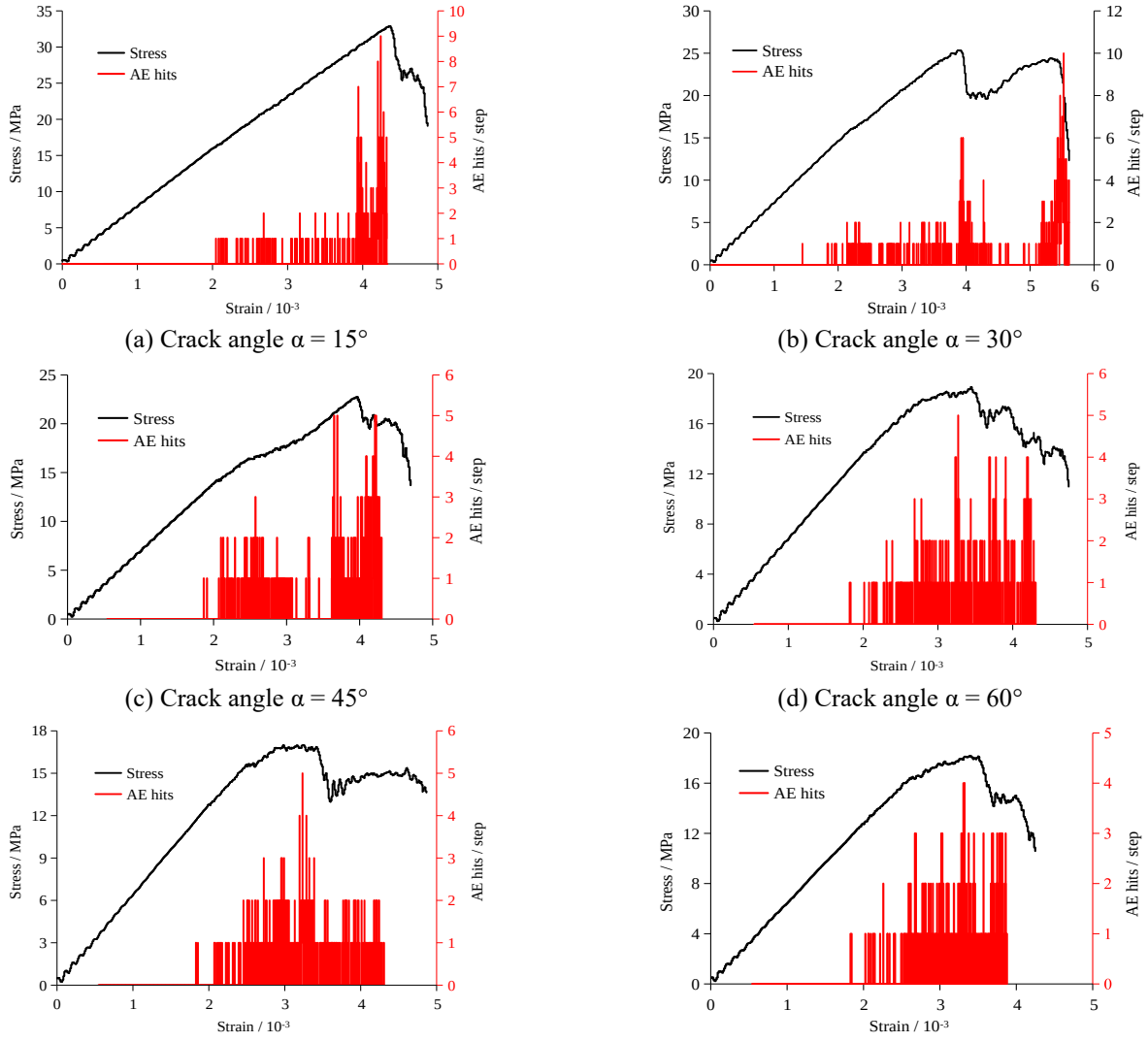

(a) Crack angle α = 15°

(b) Crack angle α = 30°

(c) Crack angle α = 45°

(d) Crack angle α = 60°

(e) Crack angle α = 75°

(f) Crack angle α = 90°

Fig. 8 Relationship between the axial stress, acoustic emission count, and strain of rock samples with different crack angle defects

first peak, a large amount of strain energy released, and the acoustic emission energy dropped sharply. As the loading test continued, the acoustic emission energy suddenly increased again, because the macroscopic cracks penetrated each other, causing overall instability and failure of sample. When cracks angle was 45°, the axial strain reached 2.1×10^{-3}, the acoustic emission count increased rapidly and kept high. This indicated that macroscopic cracks of sample appeared and continued to develop. With the progress of the loading test, the macroscopic cracks of sample penetrated each other, the stress-strain curve reached the peak, the number of acoustic emission counts increased sharply again, and instability and failure of sample occurred. Compared to the previous groups of tests with different

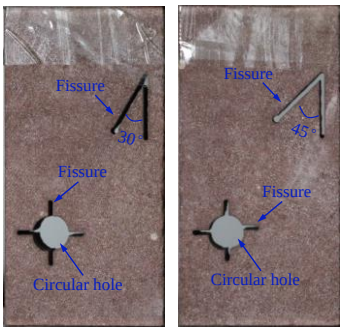

Fig. 9 Geometry of cracks defects combination in sandstone samples

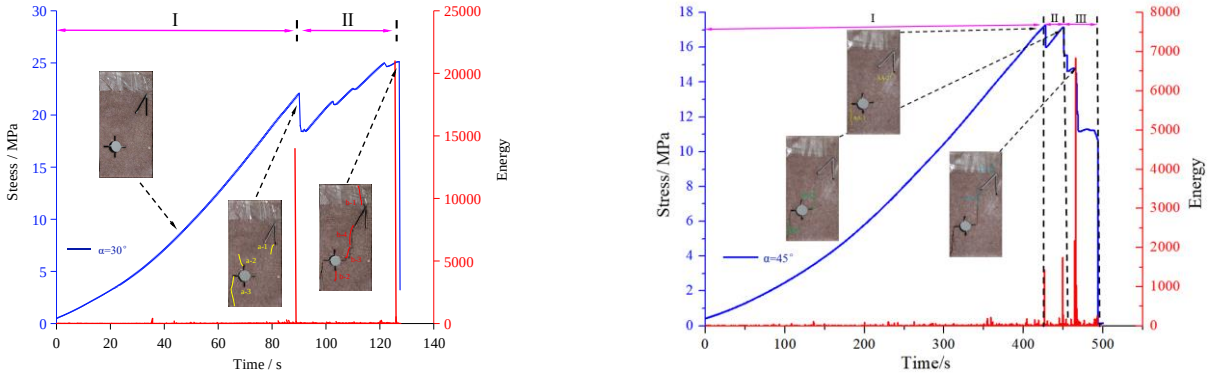

(a) α = 30° (b) α = 45°

Fig. 10 Axial stress-strain curve, acoustic emission frequency, and time relationship of combined defects

cracks angle, the stress-strain curve showed obvious plastic failure characteristics when the crack angle is 60°, and the acoustic emission count remained high for a longer time, corresponding to the more serious failure of sample when cracks angle was 60°. When the crack angle of sample is 75° and 90°, the stress-strain curve also showed the characteristics of plastic failure, but the acoustic emission energy released obviously weakened, because with increasing cracks angle, the weakening range of cracks increased, thus decreasing the energy when the sample was damaged.

The peak value of acoustic emission count decreased with increasing crack angle, corresponding to the decreasing stress with increasing crack angle, but the concentration range of acoustic emission count increased at first and then decreased with increasing crack angle. This phenomenon occurred mainly because with increasing crack angle from 15° to 60°, the weakening area increased, leading to the decrease in the overall strain energy, but the increase of the weakening range doubled the stress concentration in the local region, releasing the concentrated strain energy in this area. Therefore, the concentration range of acoustic emission increased. However, with increasing crack angle from 75° to 90°, the crack-hole combination shared part of stress at the crack-crack combination tip, decreasing the concentration range of acoustic emission.

3. Physical experiment verification

3.1 Preparation of test materials

Processing cracks defects in a real rock sample was difficult, because of many cracks in in the defect, making preparation of rock samples more difficult. Therefore, two groups of real rock samples with the cracks angle of 30° and 45° were selected for rock mechanics experiments. The physical experimental results were compared to the numerical simulation results. Red sandstone taken from a stope in Linyi City, Shandong Province was selected as the test material. In order to ensure the integrity and uniformity of sandstone, the sandstone was cut into plate-shaped samples from the same rock. In order to minimize the impact of end friction on the test results, the ratio of the height to width of samples was 2 (Jessu *et al.* 2019, Germanou *et al.* 2018, Yin *et al.* 2021, Ma *et al.* 2021). The sample size was 100 mm in height, 50 mm in width, and 20 mm in thickness. The high-pressure water jet cutting machine was used to cut samples, and the geometric parameters of cracks and circular holes were consistent with the numerical model. The sandstone samples are shown in Fig. 9.

3.2 Test procedure and rock strength and deformation behavior

The uniaxial compression test was carried out using an AG-X250 Shimadzu compression machine. Sandstone samples were tested by uniaxial compression at a constant displacement rate of 0.01 mm/s and sampling frequency of 50 Hz. The AE events in this test were monitored using an MISTRAS series PCI acoustic emission system (American Physical Acoustic Company). The system adopts a PCI-2 board with a high monitoring accuracy, low noise, low

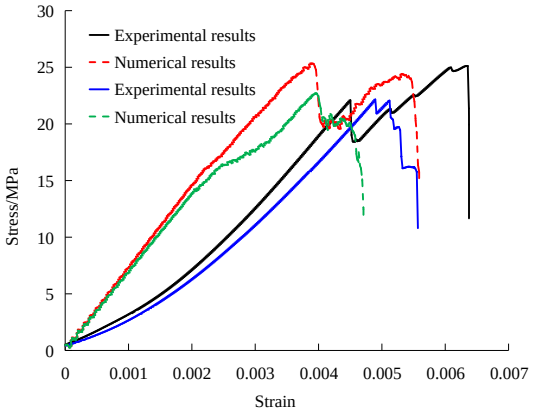

Fig. 11 Comparison of the experimental and numerical axial stress-strain curves

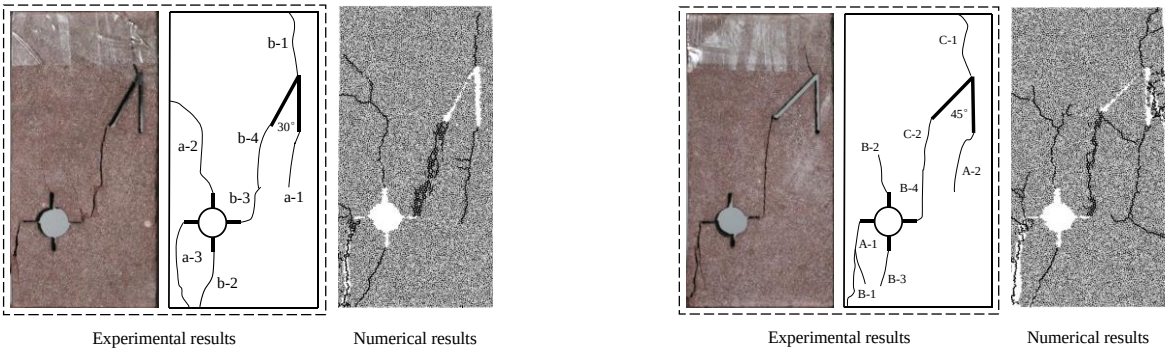

(a) α = 30° (b) α = 45°

Fig. 12 Comparison between the experimental and numerical failure when cracks angle was 30° and 45

power consumption, and complex background noise. The monitoring effect is good, and the feature parameter extraction and waveform processing can be realized simultaneously. The sampling frequency was also 50 Hz. In the process of testing, the load, deformation, and AE signals of the samples were recorded synchronously and continuously.

The stress-strain curve and failure mode of intact sandstone under uniaxial compression in Fig. 2 shows that the axial stress suddenly decreased to zero after the peak strength, indicating that the tested sample was brittle, therefore easy to break. The samples showed a nonlinear deformation relationship at the initial loading stage, mainly attributed to the closure of the original defects of samples. With increasing loading, the relationship between the axial stress and axial strain was approximately linear, and the sandstone sample showed elastic deformation. With further increase in loading, the sample entered the plastic stage and suddenly reached the peak strength. After the peak strength, macroscopic cracks of intact sample appeared rapidly, and the post-peak behavior of the stress-strain curve decreased rapidly and rock underwent failure. The uniaxial compressive strength, axial strain, and elastic modulus of sandstone were 73.6 MPa, 0.0091, and 4.89 GPa, respectively.

3.3 Cracks propagation and acoustic emission characteristics at cracks angle of 30° and 45°

When crack-crack combination was 30°, the whole loading process could be divided into two stages: the macroscopic cracks initiation and the overall instability, as shown in Fig. 10(a). In the early stage of macroscopic crack initiation, the microcracks inside the sample develop continuously with increasing loading. With further increase in loading, the internal microcracks rapidly connected and nucleated, and the macroscopic cracks begin to appear. Three macroscopic tensile cracks, a-1, a-2, and a-3 appeared from the crack-hole combination and crack-crack combination and further expanded to the bottom and upper end of the sample, resulting in instant increase in the AE signals to approximately 14,000. After entering the overall instability stage, two macroscopic tensile cracks b-1 and b-2 appeared at the intersection of the crack-crack combination and the bottom of the crack-hole combination, respectively. In the late stage of overall instability, the further connection of the new cracks b-3 and b-4 leads to the sample failure and is accompanied by the release of a large number of AE signals.

When the crack angle was 45°, the whole loading process of sample could be divided into three stages: the macroscopic cracks initiation, the macroscopic crack stable propagation, and the overall instability, as shown in Fig. 10(b). Similarly, an A-1 tensile crack was produced from the crack-hole combination and developed toward the bottom of sample, and an A-2 tensile crack was produced from the crack-crack combination toward the bottom of sample, respectively, and the AE signal instantly rises to approximately 1300. In the macroscopic crack stable

Table 3 Strength and deformation parameters of the sandstone samples in the experimental and numerical simulation experiments

Strength and deformation parameters	Angle 30°		Angle 45°	
	Experiment	Simulation	Experiment	Simulation
Peak strength	25.81	27.5	22.18	22.9
Elastic modulus	3.37	3.28	2.92	3.0
Peak strain	0.0039	0.00425	0.0049	0.0039

propagation stage, four macroscopic tensile cracks, B-1, B-2, B-3, and B-4 appeared from the crack–hole combination and crack-crack combination, and obviously more AE signals appeared in this process. After entering the overall instability stage, a C-1 tensile crack was formed at the intersection of the two prefabricated cracks and developed to the upper end of the sample, and a tensile crack C-2 was generated at the tip of the inclined prefabricated crack and developed downward and penetrated with the crack B-4, and the AE signals instantly increased to approximately 6900, destroying the sample.

The numerical model of the rock samples with the angles of 30° and 45° of crack combination defects were established and compared to the experimental test. The stress–strain curve and the failure mode were found to be similar, as shown in Fig. 11. Although the differences were observed in the peak strain, this parameter variable was acceptable.

Fig. 12 shows the failure diagram of the laboratory experiment and numerical model when crack angle was 30° and 45°, indicating that in the process of laboratory experiment and numerical experiment, cracks appeared from the cracks tip, and then continued to develop along the tip of the cracks. The crack–crack combination at the upper right side of sample and the crack–hole combination at the lower left side penetrated each other until the sample was damaged. Fig. 12 shows that the macroscopic failure characteristics of the real rock samples were similar to those of the numerical simulations when the crack angles were 30° and 45°.

Table 3 shows the comparison of strength and deformation parameters of sandstone samples obtained by experiment and numerical simulation, indicating that the peak strength of the real rock with the cracks angle of 30° and 45° was 25.11 MPa and 22.18 MPa, respectively. The peak strength achieved by the numerical experiment was 27.5 MPa and 22.9 MPa. The difference between the peak strength of the numerical experiment and the real rock was approximately 6.5% and 3.2%, respectively. The elastic modulus of the real rock was 3.37 and 2.92. The elastic modulus of the numerical experiment was 3.28 and 3.0. The difference between the numerical experiment and the real rock was approximately 2.67% and 2.74%, respectively. The peak strain of the real rock was 0.0039 and 0.0049. The difference between the numerical experiment and the real rock was approximately 8.97% and 9.96%, indicating that the peak strain of the numerical experiment was relatively different from that of the real rock sample, but they were all within a reasonable range of effect, indicating that the strength and deformation parameters of the numerical experiment and real rock samples were in good agreement with each other reflecting the strength and deformation characteristics of rock.

4. Conclusions

In conclusion, based on the discrete element program of particle flow, the mechanical properties, cracks development, and deformation and failure characteristics of cracks sand defects combination in rock were studied by numerical simulation, and the results of real rock experiment and numerical experiment were compared and analyzed, leading to the following conclusions.

• Different prefabricated cracks angle had a significant effect on the mechanical parameters of rock samples under uniaxial compression, deteriorating the mechanical properties of rock. The peak strength, peak strain, and elastic modulus of rock decreased with increasing crack angle, but increased when crack angle was 90°. The stress-strain curve gradually flattened during the plastic stage, and multiple peaks appeared after the peak, showing a jagged shape.

• Defective red sandstones with different cracks angle began to crack at the upper and lower ends of the cracks-hole combination and the crack-crack combination. With increasing crack angle from 15° to 60°, the sample underwent overall failure, the total number of cracks increased, and the spalling phenomenon gradually appeared. However, with increasing crack angle from 75° to 90°, the total number of cracks decreased and the spalling phenomenon slowed down.

• The evolution characteristics of acoustic emission were closely related to the stress–strain curve. With increasing crack angle, the peak value of acoustic emission count decreased gradually, while the concentration range of acoustic emission count increased at first and then decreased with increasing cracks angle.

• A comparison between the laboratory test and simulation test indicated that the failure strength and the final cracks propagation shape of the samples were in good agreement, verifying the accuracy of simulation test.

Acknowledgments

This study was supported by “A Project of Shandong Province Higher Educational Science and Technology Program” (J13LG08).

Conflicts of interest

The authors declare no conflicts of interest.

References

Afolagboye, L.O., He, J.M. and Wang, S.J. (2017), "Experimental study on cracking behaviour of moulded gypsum containing two non-parallel overlapping flaws under uniaxial compression", *Acta Mech. Sinica*, **33**(2), 394-405. https://doi.org/10.1007/s10409-016-0624-9.

Aharonov, E. and Karcz, Z. (2019), "How stylolite tips crack rocks", *J. Struct. Geol.*, **118**, 299-307. https://doi.org/10.1016/j.jsg.2018.11.002.

Asadizadeh, M., Moosavi, M. and Hossaini, M.F. (2018), "Investigation of mechanical behaviour of non-persistent jointed blocks under uniaxial compression", *Geomech. Eng.*, **14**(1), 29-42. https://doi.org/10.12989/gae.2018.14.1.029.

Bastola, S. and Cai, M. (2019), "Investigation of mechanical properties and crack propagation in pre-cracked marbles using lattice-spring-based synthetic rock mass (LS-SRM) modeling approach", *Comput. Geotech.*, **110**, 28-43. https://doi.org/10.1016/j.compgeo.2019.02.009.

Bratov, V. and Krivtsov, A. (2019), "Analysis of energy required for initiation of inclined crack under uniaxial compression and mixed loading", *Eng. Fract. Mech.*, **216**, 106518. https://doi.org/10.1016/j.engfracmech.2019.106518.

Chen, B, Zhang, S.C, Li, Y.Y, Li, Z.K and Zhou, H.J (2020), "Physical simulation study of crack propagation and instability information discrimination of rock-like materials with faults", *Arab. J. Geosci.*, **13**(18), 1-14. https://doi.org/10.1007/s12517-020-05966-8.

Chen, S.J., Xia, Z.G. and Yin, D.W. (2020), "Numerical study on strength and failure characteristics of rock samples with different hole defects", *B. Eng. Geol. Environ.*, 1-18. https://doi.org/10.1007/s12517-020-05966-8

Cho, N, Martin, C.D and Sego, D.C. (2007), "A clumped particle model for rock", *Int. J. Rock Mech. Min. Sci.*, **44**(7), 997-1010. https://doi.org/10.1016/j.ijrmms.2007.02.002.

Cundall, P.A. and Strack, O.D. (2008), "A discreate numerical model for granular assemblies", *Geotechnique*, **29**(1), 47-65. https://doi.org/10.1680/geot.1980.30.3.331.

Damaskinskaya, E.E., Hilarov, V.L., Panteleev, I.A., Gafurova, D.R. and Frolov, D.I (2018), "Statistical regularities of formation of a main crack in a structurally inhomogeneous material under various deformation conditions", *Phys. Solid State,* **60**(9), 1821-1826. https://doi.org/10.1155/2018/7065029.

Du, M.R, Jing, H.W., Su, H.J. and Zhu T.T. (2016), "Experimental study of strength and failure characteristics of sandstone containing prefabricated elliptical hole", *J. China U. Min. Technol.*, **45**(6), 1164-1171. https://doi.org/10.13247/j.cnki.jcumt.000593.

Germanou, L., Ho, M.T. and Zhang, Y.H. (2018), "Intrinsic and apparent gas permeability of heterogeneous and anisotropic ultra-tight porous media", *J. Nat. Gas Sci. Eng.*, **60**, 271-283. https://doi.org/10.1016/j.jngse.2018.10.003.

Gratchev, I., Dong, H.K. and Chong, K.Y. (2016), "Strength of rock-like specimens with preexisting cracks of different length and width", *Rock Mech. Rock. Eng.*, **49**(11), 4491-4496. https://doi.org/10.1007/s00603-016-1013-1.

Haeri, H., Khaloo, A. and Marji, M.F. (2015), "Fracture analyses of different pre-holed concrete specimens under compression", *Acta Mechanica Sinica*, **31**(6), 855-870. https://doi.org/10.1007/s10409-015-0436-3.

Jessu, K.V. and Spearing, A.J.S. (2019), "Direct strain evaluation method for laboratory-based pillar performance", *J. Rock Mech. Geotech. Eng.*, **11**(4), 860-866. https://doi.org/10.1016/j.jrmge.2018.12.017.

Katcoff, C.Z. and Graham-Brady, L.L. (2014), "Modeling dynamic brittle behavior of materials with circular flaws or pores", *Int. J. Solids Struct.*, **51**(3-4), 754-766. https://doi.org/10.1016/j.ijsolstr.2013.11.004.

Lee, H.W. and Jeon, S. (2011), "An experimental and numerical study of fracture coalescence in pre-cracked specimens under uniaxial compression", *Int. J. Solids Struct.*, **48**(6), 979-999. https://doi.org/10.1016/j.ijsolstr.2010.12.001.

Li, H.Q. and Wong, L.N.Y. (2013), "Numerical study on coalescence of pre-existing flaw pairs in rock-like material", *Rock Mech. Rock Eng.*, **47**(6),2087-2105. https://doi.org/10.1007/s00603-013-0504-6.

Lisjak, A. and Grasselli, G. (2014), "A review of discrete modeling techniques for fracturing processes in discontinuous rock masses", *J. Rock Mech. Geotech. Eng.*, **6**(4), 301-314. https://doi.org/10.1016/j.jrmge.2013.12.007.

Liu, T., Lin, B.Q. and Yang, W. (2017), "Mechanical behavior and failure mechanism of pre-cracked specimen under uniaxial compression", *Tectonophysics*, **712-713**, 330-343. https://doi.org/10.1016/j.tecto.2017.06.004.

Liu, W., Zhang J.P., Liu, L.M., Zhang F.T. and Mao, H.K. (2019), "Experimental study on freezing thermal parameters and uniaxial compression of weathered rock and soil in Yuandatan coal mine", *J. Shandong U. Sci. Technol. Nat. Sci.*, **38**(5), 31-38.

Lv, Y.W., Sun, C.P. and Shen, B.T. (2019), "Experimental study on damage evolution and crack propagation characteristics of sandstone under combined stress state", *J. Shandong U. Sci. Techno. (Nature Science)*, **39**(1), 37-45.

Ma, Q., Tan, Y., Liu, X., Gu, Q. and Li, X. (2020), "Effect of coal thicknesses on energy evolution characteristics of roof rock coal-floor rock sandwich composite structure and its damage constitutive model", *Compos. Part B Eng.*, **198**, 108086. https://doi.org/10.1016/j.compositesb.2020.108086.

Mondal, S., Olsen-Kettle, L. and Gross, L. (2019), "Simulating damage evolution and fracture propagation in sandstone containing a preexisting 3-D surface flaw under uniaxial compression", *Int. J. Numer. Anal. Met.*, **43**(7), 1448-1466. https://doi.org/10.1002/nag.2908.

Morgan, S.P. and Einstein, H.H. (2017), "Cracking processes affected by bedding planes in opalinus shale with flaw pairs", *Eng. Fract. Mech.*, **176**, 213-234. https://doi.org/10.1016/j.engfracmech.2017.03.003.

Saadati, M., Forquin, P. Weddfelt, K. and Larsson, P.L. (2016), "On the tensile strength of granite at high strain rates considering the Iinfluence from preexisting cracks", *Adv. Mater. Sci. Eng.* https://doi.org/10.1155/2016/6279571.

Sarfarazi, V., Haeri, H. and Shemirani, A.B. (2018), "Simulation of fracture mechanism of pre-holed concrete model under Brazilian test using PFC3D", *Smart Struct. Syst.*, **22**(6), 675-687. https://doi.org/10.12989/sss.2018.22.6.675.

Shi, H., Song, L., Zhang H. Q., Xue, K.K., Yuan, G.T., Wang Z.S. and Wang, G.Z. (2019), "Numerical study on mechanical and failure properties of sandstone based on the power-law distribution of pre-crack length", *Geomech. Eng.*, **19**(5), 421-434. https://doi.org/10.12989/gae.2019.19.5.421.

Vahab, S., Hadi, H. and Alireza, B.S. (2018), "Simulation of fracture mechanism of pre-holed concrete model under Brazilian test using PFC3D", *Smart Struct. Syst.*, **22**(6), 675-687. https://doi.org/10.12989/sss.2018.22.6.675.

Wong, R.H. and Lin, P. (2015), "Numerical study of stress distribution and crack coalescence mechanisms of a solid containing multiple holes", *Int. J. Rock Mech. Min. Sci.*, **79**, 41-54. https://doi.org/10.1016/j.ijrmms.2015.08.003.

Wong, R.H.C., Lin, P. and Tang, C.A. (2006), "Experimental and numerical study on splitting failure of brittle solids containing single pore under uniaxial compression", *Mech. Mater.*, **38**(1), 142-159. https://doi.org/10.1016/j.mechmat.2005.05.017.

Xia, Z.G., Chen, S.J., Liu, X.Z. and Sun, R. (2020), "Strength characteristics and fracture evolution of rock with different shapes inclusions based on particle flow code", *Geomech. Eng.*,

22(5), 461-473. https://doi.org/10.12989/gae.2020.22.5.461.

Xu J., Haque A., Gong W., Gamage R.P. and Xu F. (2020), "Experimental study on the bearing mechanisms of rock-socketed piles in soft rock based on micro X-ray CT analysis", *Rock Mech. Rock Eng.*, **53**, 3395-3416. https://doi.org/10.1007/s00603-020-02121-3.

Xu, Z.H., Wang, W.Y., Lin, P. and Xiong, Y. (2015), "A parameter calibration method for PFC simulation: Development and a case study of limestone", *Geomech. Eng.*, **22**(1), 97-108. https://doi.org/10.12989/gae.2020.22.1.097.

Xue, D.J. (2020), "Determination of uniaxial compressive strength of intact rock", *J. Shandong U. Sci. Technol. Nat. Sci.*, **39**(4), 28-36.

Yang, D.S., Jing, H.W., Li, Y.H. and Wang, S.Y. (2012), "An experimental study of the fracture coalescence behaviour of brittle sandstone specimens containing three fissures", *Rock. Mech. Rock. Eng.*, **45**(4), 563-582. https://doi.org/10.1007/s00603-011-0206-x.

Yin, D.W., Chen S.J., Ge Y. and Liu R, (2021), "Mechanical properties of rock–coal bi-material samples with different lithologies under uniaxial loading", *J. Mater. Res. Technol.*, **10**, 322-338. https://doi.org/10.1016/j.jmrt.2020.12.010.

Zaitsev, Y.B. and Wittmann, F.H. (1981), "Simulation of crack propagation and failure of concrete", *Mater. Struct.*, **83**(14), 357-365. https://doi.org/10.1007/BF02478729.

Zhao J.H., Chen, J.T., Zhang, X.G., Jiang, N. and Zhang, Y.Z. (2020), "Distribution characteristics of floor pore water pressure based on similarity simulation experiments", *B. Eng. Geol. Environ*. https://doi.org/10.1007/s10064-020-01835-6.

Zhu, Q.Q, Li, D.Y., Han, Z.Y., Li X.B. and Zhou, Z.L. (2019), "Mechanical properties and fracture evolution of sandstone specimens containing different inclusions under uniaxial compression", *Int. J. Rock Mech. Min. Sci.*, **115**, 33-47. https://doi.org/10.1016/j.ijrmms.2019.01.010.

CC